Electron momentum distributions in elemental semiconductors probed by positrons

Z. Tang and M. Hasegawa

Institute for Materials Research, Tohoku University, Sendai 980-8577, Japan

T. Chiba

National Institute for Research in Inorganic Materials, Namiki 1-1, Tsukuba 305-0044, Japan

M. Saito

NEC Informatec Systems, Ltd., 34, Miyukigaoka, Tsukuba 305-0841, Japan

H. Sumiya

Itami Research Laboratories, Sumitomo Electric Industries Ltd., Itami 664-0016, Japan

Y. Kawazoe and S. Yamaguchi

Institute for Materials Research, Tohoku University, Sendai 980-8577, Japan

(Received 24 October 1997)

Momentum distributions of positron-electron pairs in diamond, Si, and Ge are systematically studied using state-of-the-art techniques in experiment and theory, i.e., the positron two-dimensional angular correlation of annihilation radiation (2D-ACAR) technique and two-component density-functional (TCDF) theory. It is experimentally examined that all samples are free from positron trapping. An interesting difference among the elemental semiconductors is then clarified, namely, a flat 2D-ACAR distribution of the [001] projection in the low momentum region is found in diamond, while a deep dip is observed at the origin in Si and Ge. These experimental results are compared with those of first-principles TCDF calculations within the local-density approximation based on the scheme by Puska, Seitsonen, and Nieminen [Phys. Rev. B **52**, 10 947 (1995)] and the generalized-gradient approximation by Barbiellini *et al.* [Phys. Rev. B **53**, 16 201 (1996)]. Good agreement between theory and experiment confirms the validity of the TCDF. Analysis of calculational results clarifies that the unique electron momentum distribution in diamond is due to the carbon *p* orbital sharply localized in real space. [S0163-1829(98)06519-9]

I. INTRODUCTION

Elemental semiconductors are technologically important materials.[1] Today's semiconductor industry is in large part due to the many useful properties of Si. Diamond is a candidate for a new age material because of its unique properties of electric-field emission, wide gap, extraordinary hardness, and so on.[2] In addition to the technological merits, there is physical interest in these semiconductors since they are typical covalent crystals and are fundamental. In particular, diamond has considerably strong covalent bonds, and has unique electron distribution in real space, i.e., it has been theoretically[3] and experimentally[4] shown that there are remarkable double humps along the carbon-carbon bond, while there is a maximum at the bond center in Si and Ge. It is tempting that these features of electronic states studied in real space are examined in momentum space.

The positron two-dimensional angular correlation of annihilation radiation (2D-ACAR) technique is a powerful tool to probe electron distribution in momentum space: The observed electron momentum distribution is that sampled by the positron and projected into a chosen plane.[5] The technique has been established as a tool to determine the Fermi surface in metals, and has also provided useful information on electronic structures in semiconductors.[5–9] Early one-dimensional (1D) ACAR[10] and later 2D-ACAR (Refs. 6,7,

and 11–13) indeed revealed the important feature of electron momentum distribution for elemental semiconductors. Experiments on the perfect crystals presented prominent anisotropy, in sharp contrast to the nearly isotropic distribution in the case of positron trapping by defects.[11–14] Due to this difference in the momentum distribution, the technique allows us to evaluate the quality of samples efficiently.[11–15] Moreover, an interesting chemical trend for elemental semiconductors has been discussed. The reconstructed three-dimensional (3D) momentum distribution on the (110) plane through the Γ point shows a much flatter structure in the low momentum region in case of diamond, while a dip appears at the origin in Ge.[16] This prominent difference between diamond and Ge is expected to be due to the unique electronic structure of diamond, though the flat distribution in diamond was considered to be due to positron trapping or positronium formation in an early stage.[7]

A variety of interesting features of the observed momentum distributions have stimulated theoretical studies.[17–22] The observed anisotropy was successfully explained in terms of the selection rule based on the group theory:[20] As a consequence of the high symmetry of electron wave functions in special directions, the existence of zero momentum-density bands (cancellation of atomic orbitals[19]) decreases the partial momentum density (in a certain part of momentum space) and induces the anisotropy. References 21 and 22 discussed

the unique momentum distribution in diamond compared with those of Si and Ge. In both references it was found that the upper (*p* character) valence-band contribution to the momentum density is different between diamond and other elemental semiconductors. Reference 21 attributed the unique momentum distribution of diamond to the small lattice constant and a weak electron-positron correlation effect in diamond. In an early stage, Fujiwara, Hyodo, and Ohyama[18] discussed the electron-positron correlation effect on the momentum distribution, but the method to treat the effect in an *ab initio* way only became available very recently.[23,24] Although two-component density functional (TCDF) calculations have been applied by several groups,[14,21,24–29] the validity of the technique is not established, in particular for momentum distributions compared with positron lifetimes.

The aim of this paper is to present precise and systematic information on the electron momentum distribution for diamond, Si, and Ge. For this purpose, we employ state-of-the-art techniques in both experiment and theory, i.e., 2D-ACAR experiments and first-principles TCDF calculations. This work includes the following three highlights. First, the momentum distribution in the elemental semiconductors is observed by performing systematic experiments in order to confirm the above-mentioned chemical trend. Careful attention is paid to the quality of samples by checking there is no positron trapping. We accumulate 2D-ACAR data for diamond, Si, and Ge by varying integration axes, and provide detailed information on the momentum distributions. Second, the accumulated experimental results are compared with first-principles calculations. We employ the TCDF calculation within the local-density approximation (LDA) (Refs. 23 and 24) and generalized-gradient approximation (GGA).[27] Good agreement between theory and experiment confirms the validity of the TCDF theory. Finally, the physical origin of the observed chemical trend is discussed based on the calculational results. The unique electron distribution of diamond in both real and momentum space is attributed to the carbon *p* orbital sharply localized in real space.

The organization of this paper is as follows. The experimental procedure and calculational method are described in Secs. II and III, respectively. Experimental results are presented, and are then compared with theoretical ones in Sec. IV A. The physical origin of the chemical trend observed in the experiment is discussed based on calculational results in Sec. IV B. Section V gives a summary.

II. EXPERIMENTS

In this work, a synthetic diamond crystal of type IIa, grown by the temperature gradient method at high pressures and temperatures,[30] an undoped floating-zone-grown Si crystal, and a high-purity Ge crystal were employed for positron experiments. The 2D-ACAR measurements were performed by using the machine of Anger camera type at the National Institute for Research in Inorganic Materials, Japan. A general description of the details of the experimental setup can be found in our previous works.[11–13] The measured 2D-ACAR spectrum is proportional to the projection of the 3D momentum density $\rho(\mathbf{p})$ of the positron-electron pair along a selected axis p_z (projection direction),

$$N(p_x, p_y) \propto \int \rho(\mathbf{p}) dp_z. \tag{1}$$

In our experiments, three crystallographic directions [001], [110] and [111] are chosen as projection directions. The measured 2D-ACAR distributions were smoothed to correct for an anisotropic geometrical resolution to have an almost isotropic angular resolution of about 1.1 mrad. It is stressed here that highly perfect crystals are essential to probe the electronic structures of elemental semiconductors, especially for diamond, since the measured 2D-ACAR shape can be easily affected by positron trapping at defects. We measured 2D-ACAR spectra for many diamond crystals of various types, namely, natural crystals of types Ia and IIa and synthetic crystals of types Ib and IIa. As a result, it is found that only the synthetic IIa shows no positron trapping.[15] In other diamond crystals, the 2D-ACAR spectra have a narrow and nearly isotropic component, which is believed to be due to trapped positrons annihilating at vacancies, a vacancy-nitrogen complex, or nitrogen aggregations in the crystals.

III. CALCULATIONS

In this section, a calculational method based on the TCDF theory is described.[23,24] In Sec. III A, we outline how the positron-electron pair momentum distribution [$\rho(\mathbf{p})$] is calculated based on the TCDF. We restrict ourselves within the LDA. In Sec. III B, we give details of the electron-positron correlation function and enhancement factor based on the LDA and GGA. Calculational lifetimes of the LDA and GGA are then compared with experiments to check validities of both approximations.

A. Outline

Based on the TCDF calculation, the total energy for the interacting system of electrons and a single positron is given by the following functional over electron and positron densities:

$$E[n_v^e, n^p] = F^e[n_v^e] + F^p[n^p] - \int \frac{n_v^e(\mathbf{r})n^p(\mathbf{r}')}{|\mathbf{r}-\mathbf{r}'|} d\mathbf{r}\, d\mathbf{r}'$$
$$+ E_c^{e\text{-}p}[n_c^e + n_v^e, n^p], \tag{2}$$

where the (valence) electron and positron parts are given by the following equations:

$$F^e[n_v^e] = T[n_v^e] + \frac{1}{2} \int \frac{n_v^e(\mathbf{r})n_v^e(\mathbf{r}')}{|\mathbf{r}-\mathbf{r}'|} d\mathbf{r}\, d\mathbf{r}' + E_{xc}[n_v^e]$$
$$+ V_{ion}^e[n_v^e] \tag{3}$$

and

$$F^p[n^p] = T[n^p] + \int v_{ion}^p(\mathbf{r}) n^p(\mathbf{r}) d\mathbf{r}. \tag{4}$$

In the above equations, n_c^e, n_v^e, and n^p denote the densities of the core electrons, valence electrons, and positron, respectively, and $T[n]$ denotes the kinetic energy. The core electrons are assumed to be frozen. In the LDA, the electron-positron correlation energy functional $E_c^{e\text{-}p}$ is replaced by the

total-energy increase when a single positron is introduced in the homogeneous electron gas, and the electron exchange-correlation energy E_{xc} is approximated by that for the homogeneous electron-gas system.[31] In order to include the ion-core effect, we employ the nonlocal norm-conserving pseudopotential (V_{ion}^e) for (valence) electrons,[32] particularly constructed to optimize the softness of the pseudopotential,[33] and the Coulomb potential from the frozen-core electron charge and the nuclear point charge for the positron (v_{ion}^p).

The variation of the above energy functional [Eq. (2)] over the electron and positron densities determines the total energy of the ground state according to the density-functional theory.[34] We follow Kohn and Sham in the variational calculation.[35] The variation then leads to self-consistent single-particle equations for both electrons and positron, and band-structure calculations for the single particles are performed. In these calculations, we employ a plane-wave basis set[36] whose maximum kinetic energy is 210 (600) eV for Si and Ge (diamond). The experimental lattice constants (a) of 3.56, 5.43, and 5.66 Å are employed for diamond, Si, and Ge, respectively. The Brillouin-zone integration in the electronic band-structure calculation is performed using two special k points following Chadi and Cohen.[37] The iterative minimization technique is employed in obtaining eigenvalues.[38]

The above variational equation for the total energy determines the densities and wave functions of both electrons and positron for the ground state. Using these obtained densities and wave functions, we calculate the 3D momentum distribution of positron-electron pairs as follows:

$$\rho(\mathbf{p}) = \frac{\pi r_0^2 c}{8\pi^3} \sum_i^{occ.} \left| \int_\Omega e^{-i\mathbf{Gr}} u_{i\mathbf{p}'}(\mathbf{r}) \psi^p(\mathbf{r}) \sqrt{\gamma(\mathbf{r})} d\mathbf{r} \right|^2. \quad (5)$$

In the above equation, r_0, c, and Ω denote the classical electron radius, the speed of light, and the volume of the unit cell, respectively, and ψ^p is the positron Bloch wave function at the Γ point with the lowest energy. $u_{i\mathbf{p}'}$ is the periodical function in the electron Bloch wave function with the crystal momentum $\mathbf{p}'$ in the first Brillouin zone (FBZ): When the momentum $\mathbf{p}$ in the left-hand side in Eq. (5) is outside the FBZ, a suitable reciprocal vector $\mathbf{G}$ is chosen to place $\mathbf{p}$ by $\mathbf{p}'$ which is inside the FBZ ($\mathbf{p} = \mathbf{p}' + \mathbf{G}$). $\gamma(\mathbf{r})$ is the enhancement factor which is introduced for the correction of the single-particle wave functions (u and ψ), and is deduced from the pair distribution function at the origin for the ho-

mogeneous system which is consistent with that for the above electron-positron correlation energy.

B. Electron-positron correlation energy and enhancement factor

Here we describe details of the present electron-positron correlation energy and enhancement factor. As mentioned in Sec. III A, the electron-positron correlation energy in the LDA is defined as that of a single positron in the homogeneous electron gas. The numerical values of the correlation energy was given by Arponen and Pajanne (AP),[39] based on the correction in the random-phase approximation. The enhancement factor is deduced from numerical results of Lantto,[40] who used the hypernetted-chain approximation for the above homogenous system. These functions are first parametrized by Boroński and Nieminen,[23] and recently reparametrized by Puska, Seitsonen, and Nieminen (PSN).[24] In this study, we adopt the scheme of PSN.

In addition to the above LDA scheme, we also employ the GGA one in this study. When the enhancement factor of Lantto's type is replaced by that deduced from results of AP, the calculated lifetimes are systematically shorter than experiments,[27] though the calculation by AP is considered to be more accurate for the homogeneous system than that by Lantto. Barbiellini et al.[27] thus introduced the GGA for the correction of this scheme: One adjustable parameter α is introduced in order to include weakening of screening effects in realistic *inhomogeneous* gas systems: $\gamma^{GGA} = 1 + (\gamma^{AP} - 1)e^{-\alpha\epsilon}$ and $V_{e\text{-}p}^{GGA} = V_{e\text{-}p}^{AP} e^{-\alpha\epsilon/3}$, where γ^{AP} and $V_{e\text{-}p}^{AP}$ are the functions deduced from results of AP and $\epsilon = |\delta n_e|^2/(n_e q_{TF})^2$ (q_{TF} is the local Thomas-Fermi screening length). The universal value of 0.22 for α is adopted to reproduce experimental lifetimes for a variety of materials.

Here we confirm the validity of the LDA based on the PSN interpolation and the GGA proposed by Barbiellini et al. for lifetimes in elemental semiconductors. The lifetime τ as the inverse of annihilation rate λ is calculated as

$$1/\tau = \lambda = \pi r_0^2 c \int_\Omega [n_c^e(\mathbf{r}) + n_v^e(\mathbf{r})] n^p(\mathbf{r}) \gamma(\mathbf{r}) d\mathbf{r}. \quad (6)$$

It is found that both the LDA and GGA well reproduce the experimental lifetimes (Table I). For diamond and Si, the LDA and GGA are found to give almost the same lifetimes (Table I). In case of Ge, however, the LDA is found to provide a slightly shorter lifetime than the GGA, and the GGA
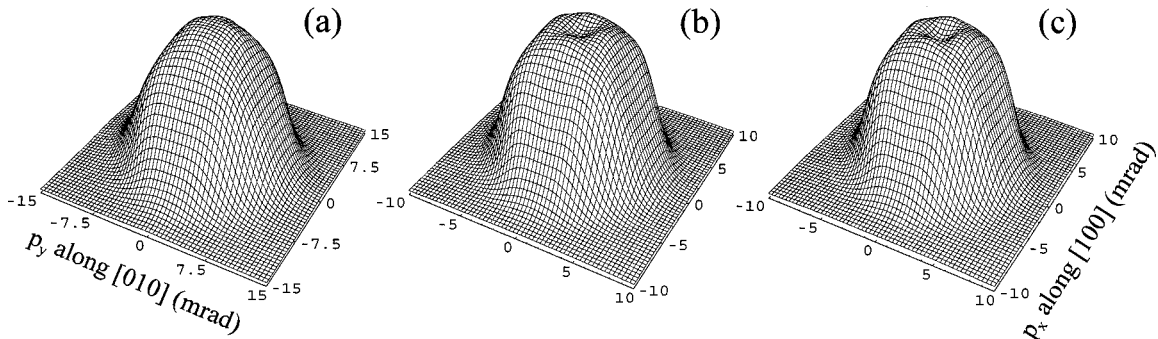

FIG. 1. Perspective plots of experimental positron 2D-ACAR distributions projected along the [001] direction in diamond (a), Si (b), and Ge (c).
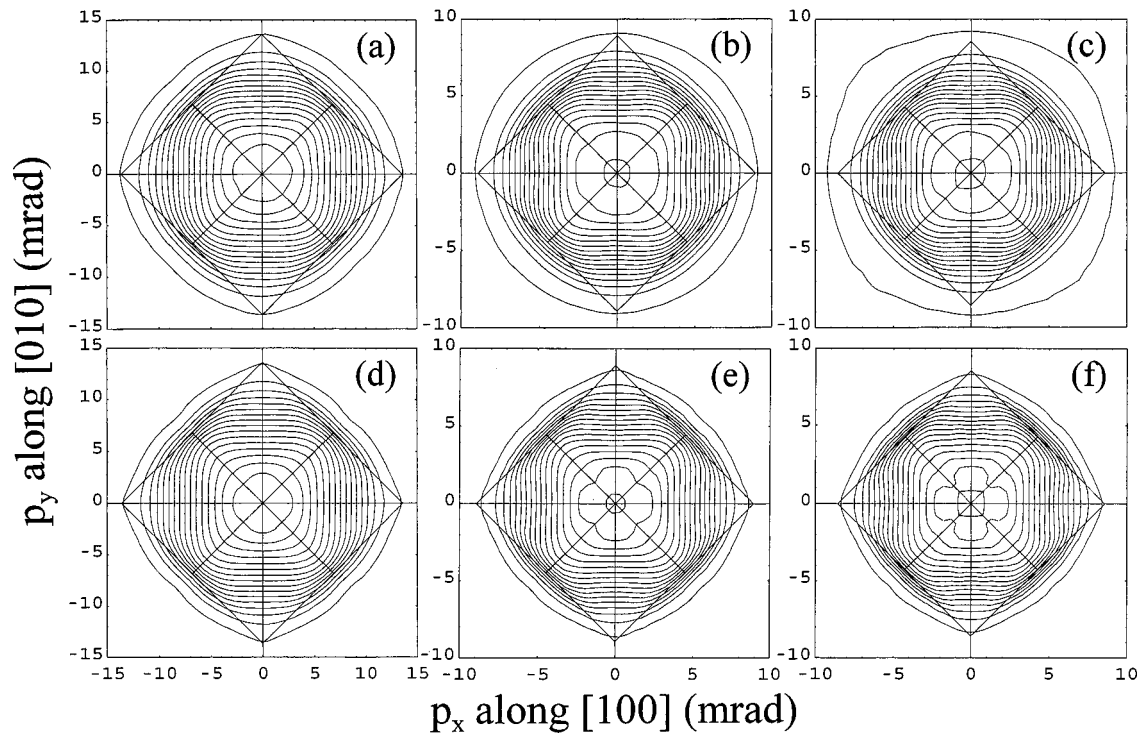
FIG. 2. Contour plots of experimental and calculational (LDA) positron 2D-ACAR distributions projected along the [001] direction in the elemental semiconductors: experimental (a) diamond, (b) Si, and (c) Ge; and calculational (d) diamond, (e) Si, and (f) Ge. The contour spacing is $\frac{1}{16}$ of the maximum value. The origin has the maximum density in both experiment (a) and calculation (d) of diamond. On the other hand, the maximum lies between the first- and second-nearest contours from the origin; that is, there is a dip at the origin, in both experiments [(b) and (c)] and calculations [(e) and (f)] of Si and Ge. The outline of the Jones zone is drawn in thin lines.
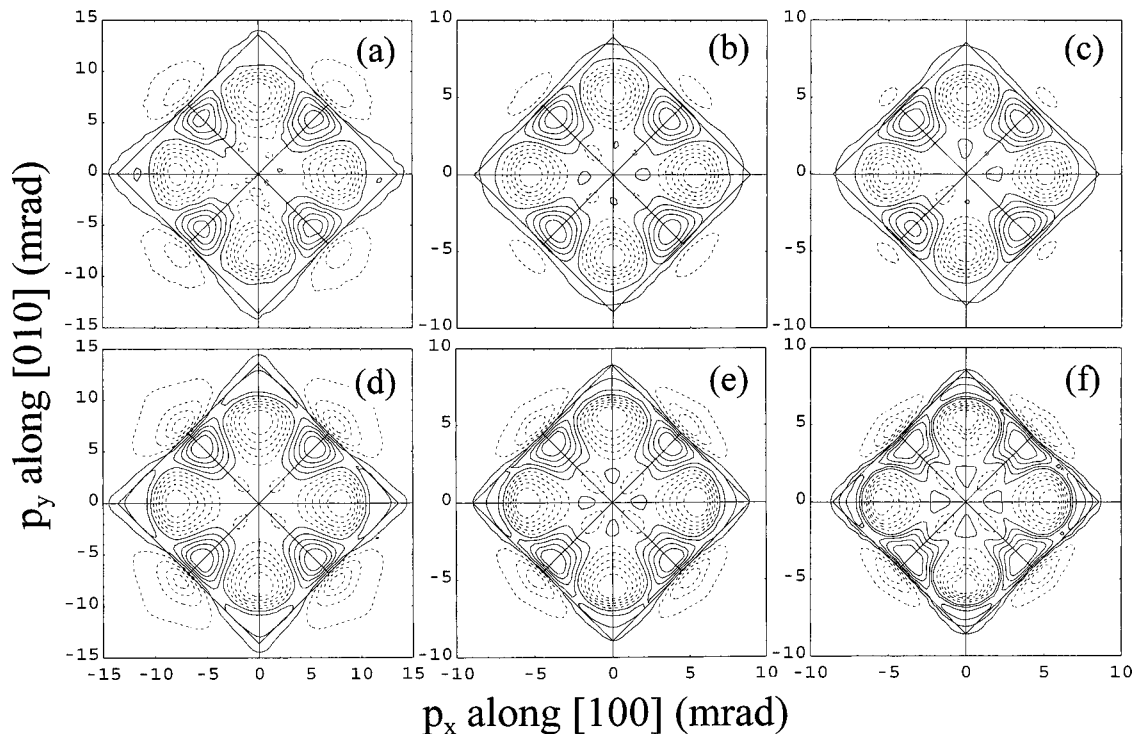

FIG. 3. Contour plots of experimental and calculational (LDA) anisotropies of the 2D-ACAR distributions projected along the [001] direction in the elemental semiconductors: experimental (a) diamond, (b) Si, and (c) Ge; and calculational (d) diamond, (e) Si, and (f) Ge. The contour spacing is one-tenth of the anisotropy amplitude. Solid (dashed) lines indicate positive (negative) values. The outline of the Jones zone is drawn in thin lines.

TABLE I. Positron lifetimes in elemental semiconductors (*ps*). The values in parentheses are the calculations based on the LMTO-ASA method (Ref. 27).

	LDA	GGA	Expt.
Diamond	93	97 (96)	103
Si	210	211 (210)	221
Ge	211	231 (228)	228

is found to give a better reproduction of the experimental value. It is finally noted that the present lifetimes based on the pseudopotential method are very close to previous ones based on the linear muffin-tin orbital method within the atomic-spheres approximation (LMTO-ASA),[27] as tabulated in Table I.

IV. RESULTS AND DISCUSSION

In this section, experimental and theoretical results are presented. The general features of positron 2D-ACAR distributions in the elemental semiconductors are discussed in Sec. IV A. In Sec. IV B, an interesting chemical trend of the low momentum distributions is discussed based on the calculations.

A. General features of positron 2D-ACAR distributions

We start with the experimental results for diamond, Si, and Ge. The perspective and contour plots of measured 2D-ACAR distributions projected along the [001] direction are shown in Figs. 1(a)–1(c) and 2(a)–2(c), respectively. It is found that the origin has a maximum intensity in diamond; a dip appears in Si and becomes slightly deeper in Ge (Figs. 1 and 2). Details of this chemical trend in the momentum distribution around the origin will be discussed in Sec. IV B. Except for the difference in the momentum distribution around the origin, the general features of 2D-ACAR distributions in these materials are found to be quite similar to each other. In particular, the 2D-ACAR distributions are very anisotropic: The momentum densities along the [100] and [110] directions are quite different from each other. This anisotropy becomes clear when the anisotropic features are brought out by extracting the anisotropy $A(p_x,p_y)$ from the observed 2D-ACAR $N(p_x,p_y)$ as
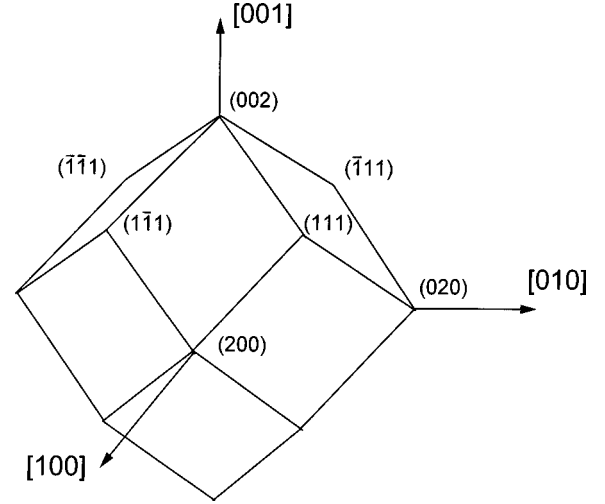
$$A(p_x,p_y)=N(p_x,p_y)-C(p_x,p_y), \qquad (7)$$

FIG. 4. The Jones zone shape of the diamond-structure lattice.

where $C(p_x,p_y)$ is a smooth cylindrical average of $N(p_x,p_y)$ around the p_z axis. Figures 3(a)–3(c) show the [001]-projected 2D-ACAR anisotropies (experimental) in the elemental semiconductors. It is seen that except for the low-momentum region around the origin, the momentum density along the [110] direction is higher than that along the [100] line inside the Jones zone presented by rectangles in Figs. 2 and 3. As a result, the distribution along the [110] direction is wider than that along the [100] direction (Table II).

The other common feature in the three samples is that the observed distribution area roughly follows the Jones zone based on the nearly-free-electron (NFE) model (Fig. 4).[10,41] According to this simple model, the 3D electron momentum distribution is unity in this zone, and is zero outside this zone. It is seen that the observed 2D momentum densities are finite within the zone, and rapidly decrease around the boundaries (Fig. 2), indicating that the NFE gives a qualitative interpretation of the 2D-ACAR distribution. We then evaluate the width of the 2D momentum distribution based on the NFE: the 3D momentum distribution (Fig. 4) is integrated along the [001] axis, and the 2D distribution on the (001) plane is obtained. The calculated full widths at half maximum (FWHM's) are comparable with experimental ones, though there is quantitative difference between theory and experiment (Table II).

Here the experimental results are compared with those of TCDF calculations. The LDA is first examined and the GGA is later applied. Good agreement between experiment and

TABLE II. The experimental and theoretical full widths at half maximum (FWHM's) (mrad) of cross sections of 2D-ACAR distributions projected along the [001] direction for elemental semiconductors. The FWHM is evaluated along [100] and [110] directions. The theoretical FWHM's are based on the LDA and GGA calculations, and their deviations (%) from the experimental values are presented in parentheses. The widths evaluated from the nearly-free-electron (NFE) model, namely, free electrons fully filling up the Jones zone, are shown together for comparison.

	[100]				[110]			
	Expt.	LDA	GGA	NFE	Expt.	LDA	GGA	NFE
Diamond	15.8	15.6 (−1.3)	15.4 (−2.5)	13.6	17.4	17.5 (+0.6)	17.5 (+0.6)	19.3
Si	10.9	10.5 (−3.7)	10.3 (−5.5)	8.9	12.2	12.0 (−1.6)	12.0 (−1.6)	12.6
Ge	10.5	10.2 (−2.9)	9.9 (−5.7)	8.5	11.7	11.6 (−0.9)	11.6 (−0.9)	12.1

TABLE III. The experimental and theoretical (LDA and GGA) FWHM's (mrad) of cross sections of 2D-ACAR distributions projected along [110] direction for the elemental semiconductors. The deviations (%) of LDA and GGA calculations from the experiments are presented in parentheses.

	[001]			[$\bar{1}$10]		
	Expt.	LDA	GGA	Expt.	LDA	GGA
Diamond	17.2	17.4 ($+1.2$)	17.2 (0.0)	16.5	16.5 (0.0)	16.3 (-1.2)
Si	11.8	11.4 (-3.3)	11.2 (-5.1)	11.5	11.1 (-3.5)	10.9 (-5.2)
Ge	11.3	10.9 (-3.5)	10.8 (-4.4)	11.0	10.8 (-1.8)	10.6 (-3.6)

theory (LDA) is found for the 2D-ACAR distribution on the (001) plane. First, the observed chemical trend in the momentum distribution around the origin among the three samples is well reproduced by the LDA calculations (Fig. 2); there is a peak (dip) in diamond (Si and Ge). Second, the anisotropic features, which are common to the three crystals, are also well reproduced (Figs. 2 and 3): The calculations show prominent differences in the momentum density between the [100] and [110] directions. For a more qualitative discussion, we evaluate the FWHM's for the [100] and [110] directions. Good quantitative agreement between experiment and first-principles theory (LDA) is obtained (Table II): The maximum deviation is found for the three crystals along the [100] direction, with values of 1.3%, 3.7%, and 2.9% for diamond, Si, and Ge, respectively. We further examine the widths in the 2D-ACAR distributions projected into the (110) and (111) planes. Again the good agreement between theory and experiment is obtained. The maximum deviation for all these data (LDA) (Tables II–IV) are found to be 3.7%. The validity of the LDA is thus established for the distribution widths in the elemental semiconductors.[42] Finally we examine the anisotropic amplitude, which is defined as the valley-to-peak altitude relative to the peak height in the 2D distribution. The LDA well reproduces the experimental results (Table V).

We next adopt the GGA scheme. The GGA also well reproduces the observed momentum distributions (Fig. 5). However, it is seen in Fig. 5 that the deviation from the experimental value is slightly larger in the GGA than in the LDA. The GGA gives somewhat narrower distributions than the LDA (Tables II–IV), and then the maximum value of the deviation in the FWHM's between the GGA calculation and experiment is found to be 7.0%, which is slightly larger than the value of 3.7% in case of the LDA. The deviation in the anisotropy amplitude from the experimental values is also slightly larger in the GGA than in the LDA (Table V). We therefore conclude that the LDA gives a somewhat better reproduction of the observed momentum distributions than

the GGA, though both methods provide successful results. Panda *et al.*[29] very recently argued that the GGA gives a slightly better reproduction of results of early 1D-ACAR experiments[10,43] than the LDA, though their results, based on the GGA and LDA, were very close to each other. The present assessment of the two calculational methods, which is based on a comparison with the up-to-date 2D-ACAR experiment, is expected to be more justified.

B. Chemical trend in the momentum distributions

As described in Sec. IV A, the present experiment clarifies the prominent chemical trend among the three crystals, and this feature is well reproduced by TCDF calculations. It is confirmed that the origin has a peak in diamond; a dip appears at the origin in Si, and the dip becomes slightly deeper in Ge. The physical reason for the chemical trend is discussed here based on calculational results.[44] In order to simplify the argument, we first investigate 3D momentum densities on the (010) plane (Fig. 6). The chemical trend is again seen along the [101] direction: There are dips at the origin in Si and Ge, and the origin is peaked in diamond. It is emphasized here that only the first lowest band has nonzero momentum density at the Γ point, and the first and third lowest bands have nonzero contributions along the [101] direction (the Γ-K-X' line) (Fig. 7). As shown in Fig. 7, the momentum density of the third band increases as the momentum increases along the [101] direction from the Γ point, and has a peak between K and X', while the first band contribution has the maximum at the origin, and decreases as the momentum increases. It is clear that the third band contribution in diamond (Si and Ge) is small (large), and therefore induces the peak (dip) at the origin.

In order to find the reason for the small contribution of the third band in diamond, here we analyze the electron wave functions based on the linear combination of atomic orbitals (LCAO) consisting of s and p orbitals.[19,45] We first argue why the momentum density of the third lowest band be-

TABLE IV. The experimental and theoretical (LDA and GGA) FWHM's (mrad) of cross sections of 2D-ACAR distributions projected along [111] direction for the elemental semiconductors. The deviations (%) of LDA and GGA calculations from the experiments are presented in parentheses.

	[$\bar{1}$10]			[$\bar{1}\bar{1}$2]		
	Expt.	LDA	GGA	Expt.	LDA	GGA
Diamond		16.8	16.4		16.8	16.5
Si	11.4	11.1 (-2.6)	10.6 (-7.0)	11.6	11.4 (-1.7)	11.1 (-4.3)
Ge		10.9	10.3		11.3	10.9

TABLE V. The experimental and theoretical anisotropy amplitudes (%) of the anisotropic components $A(p_x,p_y)$ in the 2D-ACAR distributions $N(p_x,p_y)$ with the projection direction p_z along the [001] axis for the elemental semiconductors. The anisotropy amplitude is defined as the valley-to-peak altitude of $A(p_x,p_y)$ relative to the peak height of $N(p_x,p_y)$. The theoretical values are based on the LDA and GGA calculations.

	Expt.	LDA	GGA
Diamond	13.5	14.3	15.5
Si	17.7	18.4	20.9
Ge	17.4	17.3	20.7

comes large as the momentum increases from the Γ point along the Γ-X' line. The wave function of this band at the Γ point consists of p orbitals whose phases of the two atoms are opposite to each other, and therefore the contributions of the two atoms are cancelled, i.e., the third band contributes
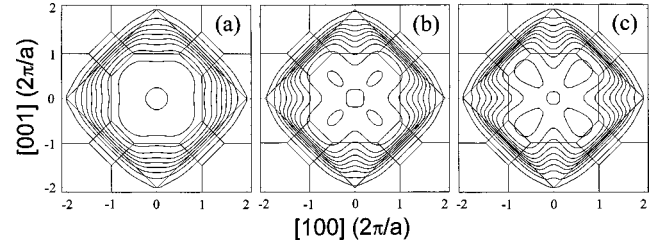

FIG. 6. Contour plots of calculational (LDA) 3D momentum distributions at the (010) plane through the Γ point in the elemental semiconductors: (a) diamond, (b) Si, and (c) Ge. The contour spacing is one-tenth of the momentum density at the Γ point. The maximum value of the contour line is set to be 1% less than the momentum density at the Γ point. The intersections of the Jones zone and Brillouin zones with this plane are shown in thin lines. The position in momentum space is represented in units of $2\pi/a$, with a being the lattice constant.

to a zero momentum density at the Γ point.[46] As the momentum increases along the [101] line, the third lowest band increases the component of $\Phi_p = \phi^1_{p[101]} + \phi^2_{p[101]}$, which has the same phase between the two atoms and therefore gives a nonzero momentum density [the suffix numbers (1 and 2) in the above expression indicate two atoms in the unit cell]. In particular, at the X' point, the wave function consists of only Φ_p. This increase of the Φ_p component is the reason why the third band contribution becomes large as the momentum increases from the Γ point (Fig. 7). In contrast, the wave function of the lowest band at the Γ point consists of an s bonding orbital ($\Phi_s = \phi^1_s + \phi^2_s$), which gives the finite momentum density. The component of Φ_s decreases in the first band as the momentum increases, leading to the maximum of the momentum density at the origin of the first band (Fig. 7).

The contributions of the first (ρ_1) and the third (ρ_3) lowest bands along the Γ-X' line are then roughly approximated by the following expressions:

$$\rho_1(\mathbf{p}) \propto \left| c_{\mathbf{p}} \int \Phi_s e^{-i\mathbf{p}\cdot\mathbf{r}} d\mathbf{r} \right|^2 = 4 \left| c_{\mathbf{p}} \int \phi_s e^{-i\mathbf{p}\cdot\mathbf{r}} d\mathbf{r} \right|^2 \quad (8)$$

and

$$\rho_3(\mathbf{p}) \propto \left| c'_{\mathbf{p}} \int \Phi_p e^{-i\mathbf{p}\cdot\mathbf{r}} d\mathbf{r} \right|^2 = 4 \left| c'_{\mathbf{p}} \int \phi_p e^{-i\mathbf{p}\cdot\mathbf{r}} d\mathbf{r} \right|^2, \quad (9)$$

where $c_{\mathbf{p}}$ and $c'_{\mathbf{p}}$ are the LCAO coefficients, and the integrations are over the whole crystal region. In deriving the above expressions, we assume that (1) the positron wave function and enhancement factor are unity in Eq. (5);[44] and that (2) inclusion by the first (third) band of the small component of Φ_p (Φ_s), which makes a minor contribution, can be neglected. According to the above equations, the momentum density is determined by the LCAO coefficient (c) and the Fourier component of the atomic orbitals. As for the LCAO coefficients, $c'_{\mathbf{p}}$ ($c_{\mathbf{p}}$) has a zero (maximum) value at the Γ point and increases (decreases) along the Γ-X' line, as was mentioned. Since these coefficients are rather insensitive to the kind of crystals, we focus on the Fourier components of the atomic orbitals in order to clarify the physical origin of the chemical trend in the total momentum distribution. In Fig. 8, we then show the Fourier components for C, Si, and
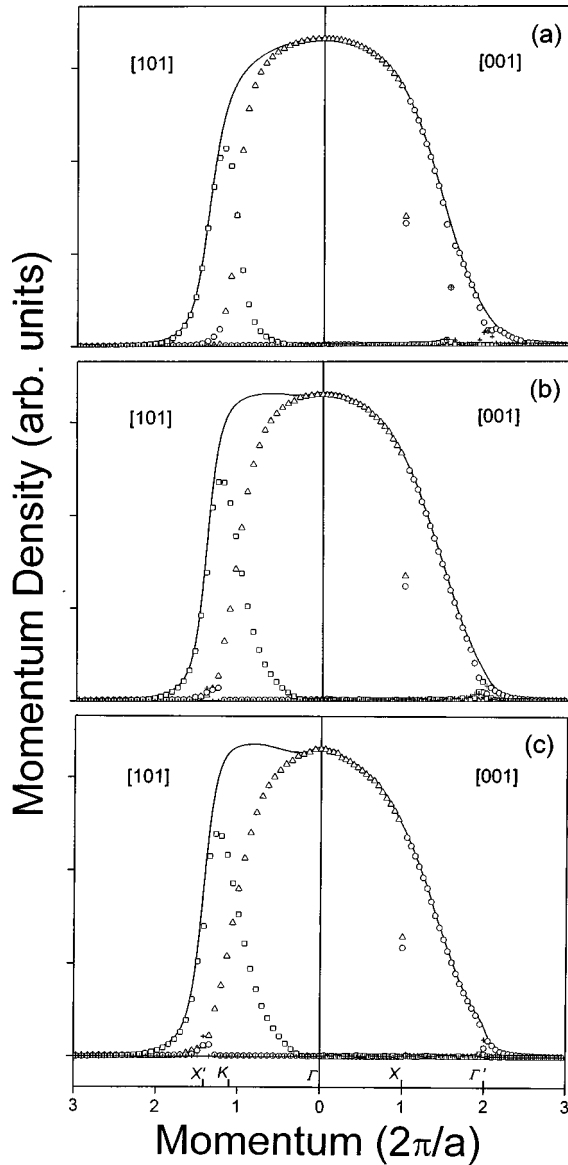

FIG. 5. Cross sections of experimental and calculational (LDA and GGA) 2D-ACAR distributions ([001] projection) along [100] and [110] directions through the origin: (a) diamond, (b) Si, and (c) Ge. The experimental and calculational 2D-ACAR distributions are normalized to the same volume. Circles, solid lines, and dashed lines denote the experiments, LDA calculations, and GGA calculations, respectively.

FIG. 7. Decomposed calculational (LDA) 3D momentum distributions along [001] and [101] crystallographic directions in the elemental semiconductors: (a) diamond, (b) Si, and (c) Ge. The momentum densities of the first, second, third, and fourth bands are represented by triangles, circles, squares, and crosses, respectively. The total momentum densities are denoted by solid lines. The total momentum densities at the Γ point in these materials are put into the same height for comparison.

Ge. It is found that the values of the p orbital of C are small in the low momentum region, and those values increase as the element becomes heavy. We therefore conclude that this small (large) values of C (Si and Ge) p orbital in momentum space is the reason why the third band contribution in diamond (Si and Ge) is small (large) along the [101] direction. The small (large) Fourier components in the low-momentum region are attributed to the localization (delocalization) in *real* space of the C (Si and Ge) p orbital. In real space, the C p orbital is very localized, since there is no core p orbital. In contrast, the valence $3p$ orbital of Si is extended as a consequence of the repulsive force due to the orthogonalization with the core $2p$ orbital. The $4p$ orbital in Ge is further extended because of the repulsive force originating from the
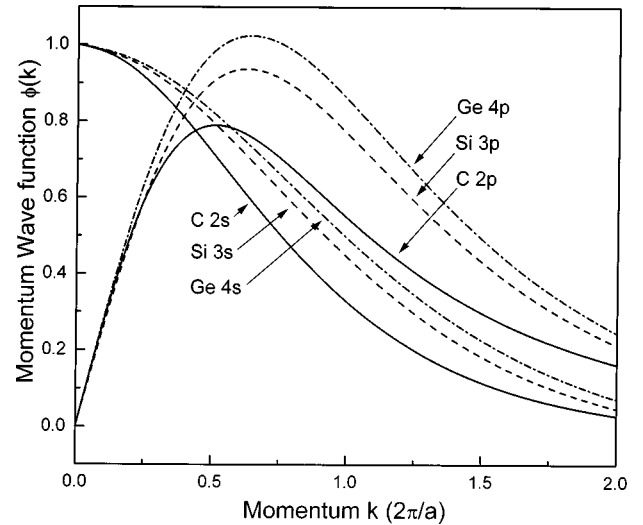

FIG. 8. Atomic momentum wave functions along the [101] direction $[\phi_{nl}(k) = c_l\sqrt{4\pi}\int_0^\infty R_{nl}(r)j_l(kr)r^2 dr$, where $R_{nl}(r)$ and $j_l(kr)$ are the *real*-space radial wave function and the spherical Bessel function, and c_l is equal to $\sqrt{1/4\pi}$ $(\sqrt{3/4\pi})$ for the s (p) state] for carbon, silicon and germanium. The momentum is represented in units of $2\pi/a$, with a being the lattice constants of diamond, Si, and Ge for atomic momentum wave functions of carbon, silicon, and germanium, respectively.

$2p$ and $3p$ core orbitals, though the weak screening of the $3d$ core orbital contributes to the shrinking of the valence orbital.

As mentioned above, the chemical trend seen in the 3D momentum distribution is explained in terms of the small (large) contribution of the C (Si and Ge) p orbital around the Γ point. We then turn to the 2D-ACAR distribution on the (001) plane. It is first noted that only first (second) lowest band contributes to the 3D momentum density along the Γ-X (X-Γ') line (the [001] direction) (Fig. 7). As a result, the 2D momentum density at the origin is the sum of the integrations of these two bands along the [001] direction. The integration of the former is larger than that of the latter, as is judged from Fig. 7. Therefore, the 2D momentum density at the origin is mainly due to the s-electron contribution, since the first band mainly consists of Φ_s. As the momentum increases from the Γ point in any direction, the p-electron contribution becomes large, since the upper band effects become large. As a consequence, the chemical trend due to the small (large) contribution of the p orbital in diamond (Si and Ge) also appears in the 2D-ACAR distributions: i.e., there is a peak at the origin in diamond, and there are dips in any direction in Si and Ge.

It is finally noted that the localized distribution of the carbon p orbital also affects the electron distribution of diamond in *real* space. As Fig. 9 shows, the x-ray-diffraction experiment[4] indicates that double humps in the bond region appear in diamond, while one peak is located at the bond center in Si. These features are well reproduced by LDA calculations (Fig. 9). We draw s and p bond charges sampled from the wave functions at the Γ point (Fig. 10). It is clearly seen that the double humps in diamond are due to the localized distribution of carbon p orbitals in real space. We thus
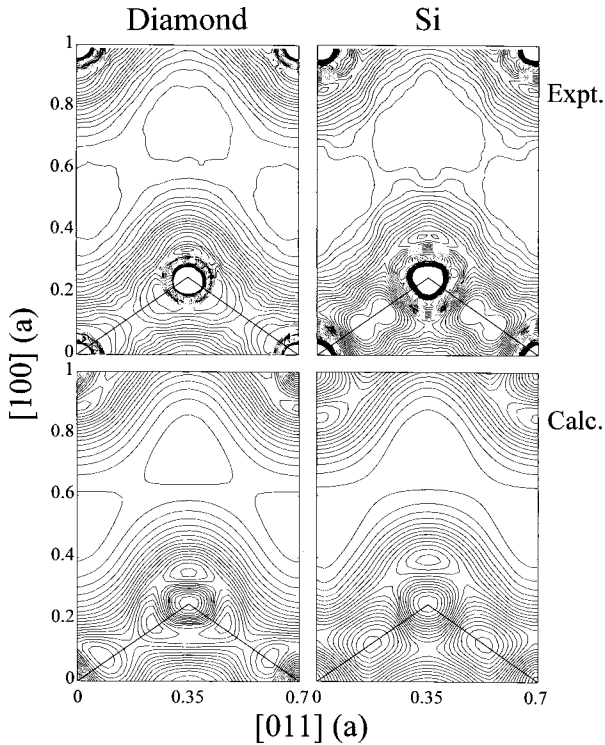
FIG. 9. Contour plots of spatial valence-charge-density distributions in the $(01\bar{1})$ plane for diamond (left panels) and Si (right panels). The x-ray-diffraction experiments (Ref. 4) (pseudopotential calculations) are shown in the upper (lower) panels. The minimum value of the contour line and the contour spacing are 2.0 and 1.0 e^-/primitive cell, respectively. The calculational charge density in core regions is not accurate due to the pseudopotential scheme. The zigzag chain is denoted by the thick lines. The position in real space is represented in units of the lattice constant a.

conclude that the unique electron distribution of diamond in both real and momentum space is due to the carbon p orbital localized in real space.

V. CONCLUSION

In conclusion, we have investigated the momentum distributions of the positron-electron pair in elemental semiconductors both experimentally and theoretically. The positron 2D-ACAR spectra in diamond, Si, and Ge have been systematically measured. It has been confirmed that the samples are free from positron trapping by defects. While all the samples show prominent anisotropy, an interesting difference among
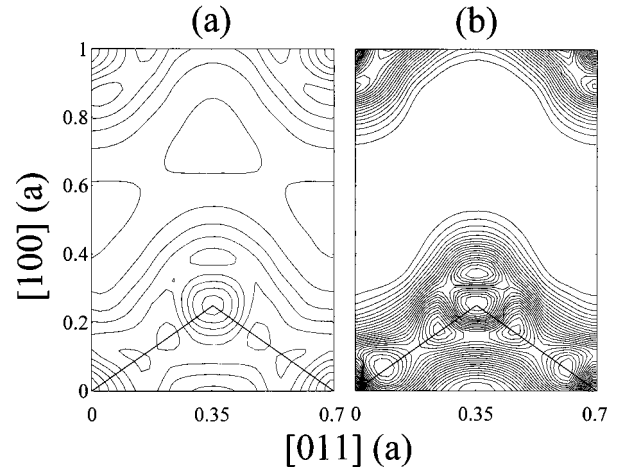

FIG. 10. Contour plots of spatial s (a) and p (b) bond charge densities in the $(01\bar{1})$ plane sampled from the wave functions at the Γ point for diamond. The minimum value of the contour line and the contour spacing in (a) [(b)] are 1.0 and 0.5 (2.0 and 1.0) e^-/primitive cell, respectively.

the elemental semiconductors has been observed, namely, a flat 2D-ACAR distribution ([001] projection) in the low-momentum region has been found in diamond, in contrast to a deep dip around the origin in Si and Ge. The accumulated experimental results have been compared with those of the first-principles TCDF calculations. We have employed the LDA scheme by Puska, Seitsonen, and Nieminen,[24] and the GGA one by Barbiellini et al.[27] The agreement between theory and experiment has confirmed the validity of the TCDF calculations. The analysis of the calculational results has clarified that the unique momentum distribution in diamond is due to the fact that the p orbital of carbon is very localized in real space compared with those of Si and Ge.

ACKNOWLEDGMENTS

[1] M. L. Cohen and J. P. Chelikowsky, in *Electronic Structure and Optical Properties of Semiconductors*, Springer Series in Solid-State Sciences Vol. 75 (Springer-Verlag, Berlin, 1988).

[2] C. Y. Fong and B. M. Klein, in *Diamond Electronic Properties and Applications*, edited by L. S. Pan and D. R. Kania (Kluwer, Boston, 1995), p. 1.

[3] M. T. Yin and M. L. Cohen, Phys. Rev. B **24**, 6121 (1981).

[4] K. Yamamoto, Y. Takahashi, K. Ohshima, F. P. Okamura, and K.

Yukino, Acta Crystallogr., Sect. A: Found. Crystallogr. **52**, 606 (1996).

[5] For example, see *Positron Spectroscopy of Solids*, edited by A. Dupasquier and A. P. Mills, Jr. (IOS, Amsterdam, 1995).

[6] R. N. West, J. Mayers, and P. A. Walters, J. Phys. E **14**, 478 (1981).

[7] S. Tanigawa, A. Uedono, L. Wei, and R. Suzuki, in *Positron Spectroscopy of Solids* (Ref. 5), p. 729; S. Tanigawa, Hyperfine

Interact. **79**, 575 (1993); S. Fujii, Y. Nishibayashi, S. Shikata, A. Uedono, and S. Tanigawa, Appl. Phys. A: Solids Surf. **61**, 331 (1995).

[8] R. Ambigapathy, A. A. Manuel, P. Hautojärvi, K. Saarinen, and C. Corbel, Phys. Rev. B **50**, 2188 (1994); R. Ambigapathy, C. Corbel, P. Hautojärvi, A. A. Manuel, and K. Saarinen, J. Phys.: Condens. Matter **7**, L683 (1995).

[9] P. Asoka-Kumar, K. G. Lynn, and D. O. Welch, J. Appl. Phys. **76**, 4935 (1994); J. P. Peng, K. G. Lynn, M. T. Umlor, D. J. Keeble, and D. R. Harshman, Phys. Rev. B **50**, 11 247 (1994).

[10] J. C. Erskine and J. D. McGervey, Phys. Rev. **151**, 615 (1966).

[11] T. Chiba, A. Kawasuso, M. Hasegawa, M. Suezawa, T. Akahane, and K. Sumino, Mater. Sci. Forum **175-178**, 327 (1995).

[12] M. Hasegawa, A. Kawasuso, T. Chiba, T. Akahane, M. Suezawa, S. Yamaguchi, and K. Sumino, Appl. Phys. A: Solids Surf. **61**, 65 (1995).

[13] M. Hasegawa, T. Chiba, A. Kawasuso, T. Akahane, M. Suezawa, S. Yamaguchi, and K. Sumino, Mater. Sci. Forum **196-201**, 1481 (1995).

[14] Z. Tang, M. Hasegawa, T. Chiba, M. Saito, A. Kawasuso, Z. Q. Li, R. T. Fu, T. Akahane, Y. Kawazoe, and S. Yamaguchi, Phys. Rev. Lett. **78**, 2236 (1997).

[15] T. Chiba, M. Hasegawa, Z. Tang, T. Akahane, A. A. Manuel, M. Saito, H. Sumiya, E. Kuramoto, and M. Takenaka, Mater. Sci. Forum **255-257**, 521 (1997).

[16] W. Liu, S. Berko, and A. P. Mills, Jr., Mater. Sci. Forum **105-110**, 743 (1992).

[17] D. Stroud and H. Ehrenreich, Phys. Rev. **171**, 399 (1968).

[18] K. Fujiwara, T. Hyodo, and J. Ohyama, J. Phys. Soc. Jpn. **33**, 1047 (1972).

[19] T. Chiba and T. Akahane, in *Positron Annihilation* , edited by L. Dorikens-Vanpraet, M. Dorikens, and D. Segers (World Scientific, Singapore, 1989), p. 674.

[20] M. Saito, A. Oshiyama, and S. Tanigawa, Phys. Rev. B **44**, 10 601 (1991).

[21] B. K. Panda, S. Fung, and C. D. Beling, Phys. Rev. B **53**, 1251 (1996).

[22] W. G. Schmidt and W. S. Verwoerd, Phys. Lett. A **222**, 275 (1996).

[23] E. Boroński and R. M. Nieminen, Phys. Rev. B **34**, 3820 (1986); M. J. Puska and R. M. Nieminen, Rev. Mod. Phys. **66**, 841 (1994); R. M. Nieminen, in *Positron Spectroscopy of Solids* (Ref. 5), p. 443.

[24] M. J. Puska, A. P. Seitsonen, and R. M. Nieminen, Phys. Rev. B **52**, 10 947 (1995).

[25] L. Gilgien, G. Galli, F. Gygi, and R. Car, Phys. Rev. Lett. **72**, 3214 (1994).

[26] M. Saito and A. Oshiyama, Phys. Rev. B **53**, 7810 (1996).

[27] B. Barbiellini, M. J. Puska, T. Korhonen, A. Harju, T. Torsti, and R. M. Nieminen, Phys. Rev. B **53**, 16 201 (1996).

[28] B. Barbiellini, M. Hakala, M. J. Puska, R. M. Nieminen, and A. A. Manuel, Phys. Rev. B **56**, 7136 (1997).

[29] B. K. Panda, W. LiMing, S. Fung, and C. D. Beling, Phys. Rev. B **56**, 7356 (1997).

[30] H. Sumiya and S. Satoh, Diamond Relat. Mater. **5**, 1359 (1996).

[31] D. M. Ceperley and B. J. Alder, Phys. Rev. Lett. **45**, 566 (1980).

[32] D. R. Hamann, Phys. Rev. B **40**, 2980 (1989); L. Kleinman and D. M. Bylander, Phys. Rev. Lett. **48**, 1425 (1982).

[33] J. S. Lin, A. Qteish, M. C. Payne, and V. Heine, Phys. Rev. B **47**, 4174 (1993); A. M. Rappe, K. M. Rabe, E. Kaxiras, and J. D. Joannopoulos, *ibid.* **41**, 1227 (1990).

[34] P. Hohenberg and W. Kohn, Phys. Rev. **136**, B864 (1964).

[35] W. Kohn and L. J. Sham, Phys. Rev. **140**, A1133 (1965).

[36] J. Ihm, A. Zunger, and M. L. Cohen, J. Phys. C **12**, 4409 (1979).

[37] D. J. Chadi and M. L. Cohen, Phys. Rev. B **8**, 5747 (1973).

[38] R. Car and M. Parrinello, Phys. Rev. Lett. **55**, 2471 (1985); M. C. Payne, M. P. Teter, D. C. Allan, T. A. Arias, and J. D. Joannopoulos, Rev. Mod. Phys. **64**, 1045 (1992).

[39] J. Arponen and E. Pajanne, Ann. Phys. (N.Y.) **121**, 343 (1979).

[40] L. J. Lantto, Phys. Rev. B **36**, 5160 (1987).

[41] P. E. Mijnarends, Phys. Rev. B **4**, 2820 (1971).

[42] The influence of the maximum kinetic energy of the plane waves and of the FBZ sampling on the 2D-ACAR distributions is checked by various computations. The results using a cutoff kinetic energy of 700 eV and ten special k points differ by less than 0.5% from the present calculations.

[43] K. Fujiwara and T. Hyodo, J. Phys. Soc. Jpn. **35**, 1133 (1973).

[44] We find the chemical trend even when the positron wave function and enhancement factor are unity, i.e., there is a peak (dip) at the origin in diamond (Si and Ge).

[45] T. Chiba, J. Chem. Phys. **64**, 1182 (1976).

[46] The nonzero momentum-density bands are generally determined using the selection rule based on the group theory, i.e., only the totally symmetric bands have nonzero momentum-density contributions, e.g., Σ_1 along the Γ-X' (the first and third bands). Details are given in Ref. 20. Since our purpose is to clarify the chemical trend, we analyze the LCAO wave functions in the text.